Am J Physiol Renal Physiol 310: F785–F795, 2016.
First published January 3, 2016; doi:10.1152/ajprenal.00488.2015.

Oxalate-induced chronic kidney disease with its uremic and cardiovascular complications in C57BL/6 mice

Shrikant R. Mulay,[1]* Jonathan N. Eberhard,[1]* Victoria Pfann,[2]* Julian A. Marschner,[1] Murthy N. Darisipudi,[2] Christoph Daniel,[3] Simone Romoli,[1] Jyaysi Desai,[1] Melissa Grigorescu,[1] Santhosh V. Kumar,[1] Birgit Rathkolb,[4,5] Eckhard Wolf,[5] Martin Hrabě de Angelis,[4,6,7] Tobias Bäuerle,[8] Barbara Dietel,[9] Carsten A. Wagner,[10] Kerstin Amann,[3] Kai-Uwe Eckardt,[2] Peter S. Aronson,[1] Hans Joachim Anders,[1]* and Felix Knauf[2,11]*

[1]Medizinische Klinik und Poliklinik IV, Klinikum der Universität München, Munich, Germany; [2]Department of Nephrology and Hypertension, Friedrich-Alexander-Universität Erlangen-Nürnberg (FAU), Erlangen, Germany; [3]Department of Nephropathology, Friedrich-Alexander-Universität Erlangen-Nürnberg (FAU), Erlangen, Germany; [4]German Mouse Clinic, Institute of Experimental Genetics, Helmholtz-Zentrum München, Neuherberg, Germany; [5]Institute of Molecular Animal Breeding and Biotechnology, Gene Center, Ludwig-Maximilians-University München, Munich, Germany; [6]School of Life Science Weihenstephan, Technische Universität München, Freising, Germany; [7]German Center for Diabetes Research (DZD), Neuherberg, Germany; [8]Preclinical Imaging Platform Erlangen, Institute of Radiology, Friedrich-Alexander-Universität Erlangen-Nürnberg (FAU), Erlangen, Germany; [9]Department of Cardiology, Friedrich-Alexander-Universität Erlangen-Nürnberg (FAU), Erlangen, Germany; [10]Zurich Center for Integrative Human Physiology, Zurich, Switzerland; and [11]Department of Internal Medicine, Yale University School of Medicine, New Haven, Connecticut

Submitted 26 October 2015; accepted in final form 11 January 2016

Mulay SR, Eberhard JN, Pfann V, Marschner JA, Darisipudi MN, Daniel C, Romoli S, Desai J, Grigorescu M, Kumar SV, Rathkolb B, Wolf E, Hrabě de Angelis M, Bäuerle T, Dietel B, Wagner CA, Amann K, Eckardt K, Aronson PS, Anders HJ, Knauf F. Oxalate-induced chronic kidney disease with its uremic and cardiovascular complications in C57BL/6 mice. *Am J Physiol Renal Physiol* 310: F785–F795, 2016. First published January 3, 2016; doi:10.1152/ajprenal.00488.2015.—Chronic kidney disease (CKD) research is limited by the lack of convenient inducible models mimicking human CKD and its complications in experimental animals. We demonstrate that a soluble oxalate-rich diet induces stable stages of CKD in male and female C57BL/6 mice. Renal histology is characterized by tubular damage, remnant atubular glomeruli, interstitial inflammation, and fibrosis, with the extent of tissue involvement depending on the duration of oxalate feeding. Expression profiling of markers and magnetic resonance imaging findings established to reflect inflammation and fibrosis parallel the histological changes. Within 3 wk, the mice reproducibly develop normochromic anemia, metabolic acidosis, hyperkalemia, FGF23 activation, hyperphosphatemia, and hyperparathyroidism. In addition, the model is characterized by profound arterial hypertension as well as cardiac fibrosis that persist following the switch to a control diet. Together, this new model of inducible CKD overcomes a number of previous experimental limitations and should serve useful in research related to CKD and its complications.

renal failure; oxalate; CKD-MBD; hypertension; cardiovascular

TRANSLATIONAL RESEARCH IN the area of chronic kidney disease (CKD) requires experimental models that *1*) can be induced in C57BL/6 mice as it represents the most commonly used genetic background for gene manipulations; *2*) reliably generate stable CKD; *3*) result in CKD within a relatively short time to limit the burden for animals and reduce housing costs; and *4*) do not require surgery to minimize animal distress and the use of anesthetic drugs or pain killers with potentially confounding effects. In addition, an ideal model should *5*) work in male and female mice with low interindividual variability to allow sex-based comparisons in response to interventions and minimize animal use; *6*) not reduce renal mass, which limits the tissue available for analysis; *7*) reduce glomerular filtration rate (GFR) by >50% to allow detection of the changes in the clinical biomarkers plasma blood urea nitrogen (BUN) and creatinine; and *8*) be associated with typical complications associated with CKD in humans, such as normochromic anemia, hyperphosphatemia, hyperparathyroidism, hyperkalemia, acidosis, hypertension, and cardiovascular disease. The present work reviews the most commonly used murine models of inducible CKD (1, 3, 12, 16) and contrasts them with a novel oxalate-induced model of stable CKD.

METHODS

Animal studies and analytic methods. Male and female 8- to 12-wk-old gender-matched C57BL/6 mice were obtained from Charles River Laboratories (Sulzfeld, Germany) and housed in groups of five mice in standard housing conditions with unlimited access to food and water. An oxalate diet was prepared by adding 50 μmol/g sodium oxalate to a calcium-free standard diet (Ssniff, Soest, Germany) as previously described (15). Removal of calcium from the diet increases the amount of soluble oxalate available for absorption as previously shown (15). An oxalate- and calcium-free diet (control diet) was given for 3 days to eliminate any residual intestinal calcium before a switch to a high-soluble oxalate diet and used after ending of the oxalate-feeding period. All experimental procedures were approved by local government authorities.

Assessment of renal injury. Mice kidney sections of 2 μm were stained with periodic acid-Schiff (PAS) reagent. Tubular injury was scored by assessing the percentage of necrotic tubules and presence of tubular casts. F4/80+ve macrophages and CD3+ve T cells (both Serotec, Oxford, UK) were identified by immunostaining and were

---

* S. R. Mulay, J. N. Eberhard, V. Pfann, H. J. Anders, and F. Knauf contributed equally to this work.

Address for reprint requests and other correspondence: F. Knauf, Dept. of Nephrology and Hypertension, Friedrich-Alexander-Universität (FAU)-Universitätsklinikum Erlangen, Schwabachanlage 12, 91054 Erlangen, Germany (e-mail: Felix.Knauf@uk-erlangen.de).

counted in 15 high-power fields (hpf) per section using ImageJ software. A similar approach was also used to quantify Silver stains. Fibrotic areas were identified by Silver stain, Masson trichrome stain, and collagen 1a1 and were quantified using ImageJ software. Serial sections of the kidney were stained with *Lotus tetragonolobus* lectin to observe atubular glomeruli. All assessments were performed by an observer blinded to the experimental condition.

RNA preparation and real-time quantitative PCR. Total RNA was isolated from kidneys using a Qiagen RNA extraction kit following the manufacturer's instructions. After quantification, RNA quality was assessed using agarose gels. From isolated RNA, cDNA was prepared using reverse transcriptase (Superscript II). Real-time RT-PCR was performed using SYBR Green PCR master mix and was analyzed with a Light Cycler 480 (Roche). All gene expression values were normalized using 18S RNA as a housekeeping gene. All primers used for amplification were from Metabion (Martinsried, Germany) and are listed in Table 1.

Hematological analysis. Hematological analysis was performed using prefilled Sysmex capillary tubes (Sysmex Deutschland, Norderstedt, Germany). An aliquot of 50 μl EDTA-blood was determined by using a 50-μl end-to-end capillary and was diluted 1:5 in 200 μl prefilled Sysmex Cellpack buffer. Diluted samples were stored at room temperature until analysis. Complete peripheral blood counts, differential leukocyte counts, and reticulocyte counts were determined with a Sysmex XT2000iV hematology analyzer (Sysmex Deutschland) in the "capillary blood" mode using the option "CBC DIFF RET" as described previously (23) with the following parameters included: total white blood cell count (WBC), total red blood cell count, platelet count, hemoglobin concentration, hematocrit, mean corpuscular volume, mean corpuscular hemoglobin content, mean corpuscular hemoglobin concentration, red cell distribution width (RDW)-coefficient of variance, mean platelet volume, platelet distribution width, platelet large cell ratio, plateletcrit, absolute cell counts and proportions of WBC for lymphocytes, monocytes, as well as neutrophil, eosinophil, and basophil granulocytes, and absolute cell counts and proportion of RDW of reticulocytes, including proportions of reticulocyte maturation states as determined by fluorescence intensity, mature low-fluorescent reticulocytes, less mature medium fluorescent reticulocytes (MFR) and very immature highly fluorescent reticulocytes (HFR), as well as the sum of MFR and HFR as immature reticulocyte fraction.

Table 1. *Primer sequences*

Target	Primer Sequence
KIM-1	Forward 5′-TCAGCTCGGGAATGCACAA-3′
	Reverse 5′-TGGTTGCCTTCCGTGTCTCT-3′
TIMP-2	Forward 5′-CAGACGTAGTGATCAGAGCCAAA-3′
	Reverse 5′-ACTCGATGTCTTTGTCAGGTCC-3′
RANTES	Forward 5′-GTGCCCACGTCAAGGAGTAT-3′
	Reverse 5′-CCACTTCTTCTCTGGGTTGG-3′
IL-6	Forward 5′-TGATGCACTTGCAGAAAACA-3′
	Reverse 5′-ACCAGAGGAAATTTTCAATAGGC-3′
Fibronectin	Forward 5′-GGAGTGGCACTGTCAACCTC-3′
	Reverse 5′-ACTGGATGGGGTGGGAAT-3′
Collagen 1a1	Forward 5′-ACATGTTCAGCTTTGTGGACC-3′
	Reverse 5′-TAGGCCATTGTGTATGCAGC-3′
FSP-1	Forward 5′-CAGCACTTCCTCTCTCTTGG-3′
	Reverse 5′-TTTGTGGAAGGTGGACACAA-3′
TNF-α	Forward 5′-CCACCACGCTCTTCTGTCTAC-3′
	Reverse 5′-AGGGTCTGGGCCATAGAACT-3′
α-SMA	Forward 5′-ACTGGGACGACATGGAAAAG-3′
	Reverse 5′-GTTCAGTGGTGCCTCTGTCA-3′
iNOS	Forward 5′-GAGACAGGGAAGTCTGAAGCAC-3′
	Reverse 5′-CCAGCAGTAGTTGCTCCTCTTC-3′
18S RNA	Forward 5′-GCAATTATTCCCCATGAACG-3′
	Reverse 5′-AGGGCCTCACTAAACCATCC-3′

SMA, smooth muscle actin; iNOS, inducible nitric oxide synthase.

Clinical chemistry analyses. Inorganic phosphate (P_i) was analyzed using an AU480 Clinical chemistry analyzer (Beckman-Coulter, Krefeld, Germany) and adapted test kits provided by Beckman Coulter in either undiluted or 1:2 with deionized water-diluted EDTA-treated plasma samples as described previously (24). Heparinized capillaries were filled with 100 μl of whole blood and subjected to measurement of potassium and pH using a blood-gas analyzer (ABL 835 Flex, Radiometer, Willich, Germany).

Blood pressure measurements. Blood pressure was measured continuously in male 10- to 12-wk-old C57BL/6 mice using an intra-arterial telemetric transmitter system as previously described (3). In brief, under isoflurane anesthesia a transmitter device (PhysioTel TA11PA-C10; Data Sciences International, St. Paul, MN) was surgically implanted into the left common carotid artery 1 wk before data sampling. The transmitter was placed subcutaneously over the abdominal area. All animals were then housed in open cages and allowed to recover for 2 wk during which mice received unlimited access to regular chow (Ssniff, Soest, Germany) and tap water. Following recovery, the diet was changed to a synthetic calcium- and oxalate-free diet (0% Ca 0% oxalate, TD. 95027, Ssniff) for 1 wk, followed by high-oxalate diet (0% Ca 0.67% oxalate, TD. 95027, Ssniff) for 8 days and thereafter a control diet for another 10 days. Blood pressure was detected and recorded continuously for 5 wk by the Dataquest A.R.T. System (Data Sciences International). Systolic and diastolic blood pressure values were calculated as an average of the last 24 h of each diet period by the Dataquest ART 4.1 software (Data Sciences International). Mean arterial pressure (MAP) was calculated from diastolic and systolic pressure values using a standard equation.

Transcutaneous measurement of GFR in conscious mice. For GFR measurement, mice were anesthetized with isoflurane and a miniaturized imager device built from two light-emitting diodes, a photodiode and a battery (Mannheim Pharma and Diagnostics), was mounted via double-sided adhesive tape onto the shaved animal's neck (26). For the duration of recording (~1.5 h), each animal was conscious and kept in a single cage. Before the intravenous injection of 150 mg/kg FITC-sinistrin (Mannheim Pharma and Diagnostics), the skin's background signal was recorded for 5 min. After removal of the imager device, the data were analyzed using MPD Lab software (Mannheim Pharma and Diagnostics). The GFR (μl/min) was calculated from the decrease in fluorescence intensity over time (i.e., plasma half-life of FITC-sinistrin) using a two-compartment model, body weight of the mouse and an empirical conversion factor (26).

Measurement of intact FGF23, parathyroid hormone (PTH), and phosphorus. The plasma concentration of intact FGF23 (Kainos Laboratories or Immutopics International) and intact PTH (Immutopics International) were measured by enzyme-linked immunosorbent assays according to the manufacturers' protocols. Phosphate was measured by the phosphomolybdate method (9, 10).

MRI. Excised kidneys ($n = 12$) from C57BL/6 male mice fed either a high-oxalate ($n = 6$ kidneys) or control diet ($n = 6$ kidneys) for 21 days were processed in 2% agarose and placed in a whole body coil for mice (Bruker, Ettlingen, Germany) of a dedicated small-animal ultra-high-field MR scanner (ClinScan 7 Tesla, Bruker). Standard sequences for morphology and mapping of T1, T2, and T2* relaxation times as well as of the apparent diffusion coefficient (ADC; Siemens, Erlangen, Germany) were performed in kidneys in a sagittal orientation (compare Fig. 5). By mapping of relaxation times, specific magnetic properties of tissues are quantified, which can be performed in multiple tissues and organs. Thereby, an increase in T1 relaxation time may be associated with fibrosis, while prolonged T2 relaxation times are found in inflammation (25). Furthermore, calculation of the ADC by diffusion-weighted imaging captures the Brownian motion of water molecules that is locally altered in pathological conditions like fibrosis, resulting in decreased water diffusion, and thus decreased ADC values (11). For postprocessing of images, three regions of interest were placed in the cortex, medulla, and transitional zone, respectively, to determine T1, T2, and T2* relaxation times as well as the ADC (Osirix, open-source software). Furthermore, the volume of the cortex was determined on morphological, T2-weighted images (Osirix, open-source software).

Histological examination of cardiac fibrosis. Hearts were excised, snap frozen in liquid nitrogen, and stored at −80°C until further use. The lower base of the left ventricle was embedded in Tissue Tec, whereupon 10-μm-thick cross sections were prepared on a SLEE-MNT cryostat (Mainz, Germany). Ventricular sections were stained for fibrotic tissue using Masson's trichrome staining (Sigma-Aldrich, Taufkirchen, Germany). Briefly, sections were fixed in 4% paraformaldehyde for 1 h at room temperature and refixed overnight in Bouin's solution. The next day, slides were washed in distilled water and incubated for 5 min with hematoxylin. After the slides were washed in distilled water for 10 min, sections were incubated for 5 min in biebrich scarlet acid fuchsin. Slides were washed three times in distilled water, after which they were incubated in phosphomolybdic acid three times each for 3 min. After 5 min of incubation with aniline blue, which leads to a blue staining of fibrotic tissue, slides were rinsed in distilled water and dehydrated in isopropanol and xylene, before they were mounted with roti-histokit (Carl Roth, Karlsruhe, Germany). Differentiation was performed by incubating the slides for 2 min in ice-cold acetic acid. After a washing step in distilled water, slides were covered with mounting medium. Microscopic composite images of the complete cross sections were obtained at ×150 mag-

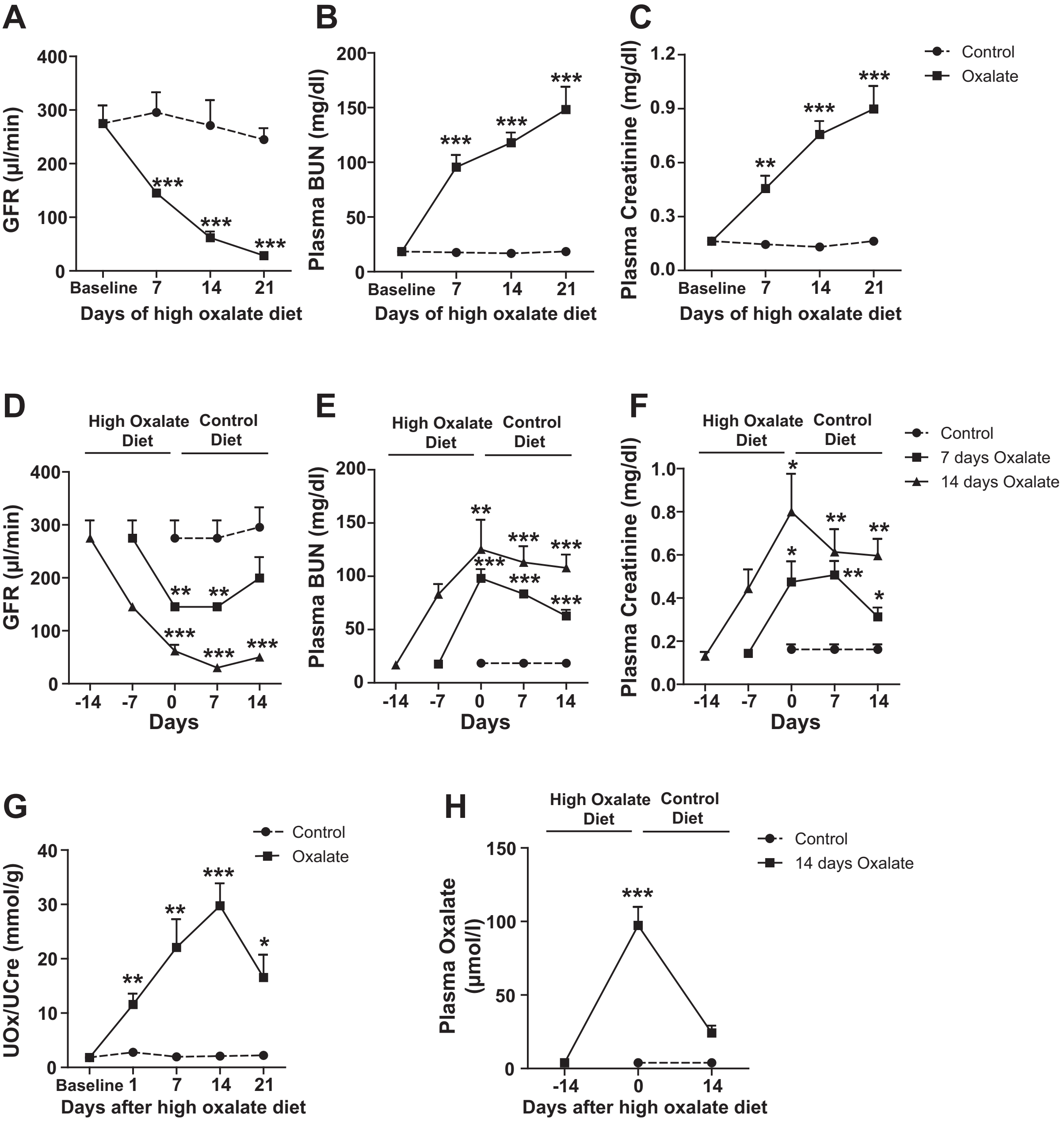

Fig. 1. A diet high in soluble oxalate induces progressive or stable chronic kidney disease (CKD). *A–C*: C57BL/6 male mice were fed either a high-oxalate or control diet for 21 days and glomerular filtration rate (GFR; *A*), plasma blood urea nitrogen (BUN; *B*), and plasma creatinine (*C*) were measured at baseline and *days 7*, *14*, and *21*. *D–F*: C57BL/6 male mice received a high-oxalate diet for 0, 7, or 14 days, respectively, and thereafter a control diet for 14 days. GFR (*D*), plasma BUN (*E*), plasma creatinine (*F*), urine oxalate (*G*), and plasma oxalate (*H*) were measured at indicated time points. Values are means ± SE from 5 mice/group. *$P < 0.05$, **$P < 0.01$, and ***$P < 0.001$ vs. control group.

nification on a light microscope (Olympus IX70, Hamburg, Germany) with an inverted CCD-camera (Nikon DXM1200, Düsseldorf, Germany). The blue-stained fibrotic area was manually quantified by an observer blinded to the experimental condition on three cross sections per heart using ImageJ software. The endocardium and trabeculae carnae were excluded from quantification. After determination of the ventricular area, the mean fibrosis content was calculated by dividing the area of trichrome-stained fibrotic fibers by total left ventricular

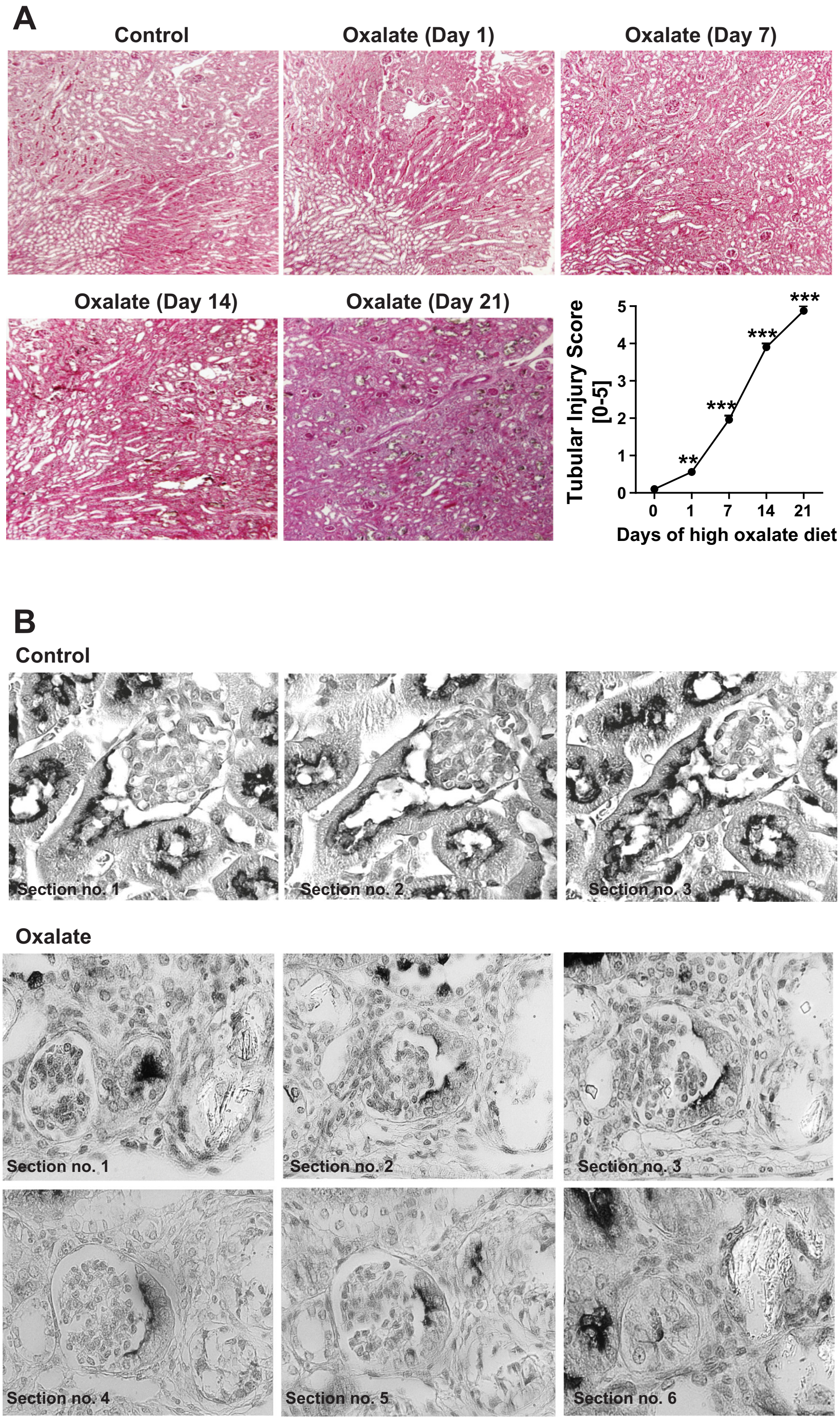

Fig. 2. Oxalate-induced CKD shows atubular glomeruli. C57BL/6 male mice were fed either a high-oxalate or control diet for 21 days. *A*: periodic acid-Schiff (PAS) staining at various time points and quantification. *B*: serial sections of the kidney were stained with *Tetragonolobus* lectin to observe atubular glomeruli. Note the atubular glomerulus (clearly separated by a membrane) is surrounded by tubules containing crystals. Values are means ± SE from 7–8 mice/group. $^{**}P < 0.01$ and $^{***}P < 0.001$ vs. control group.

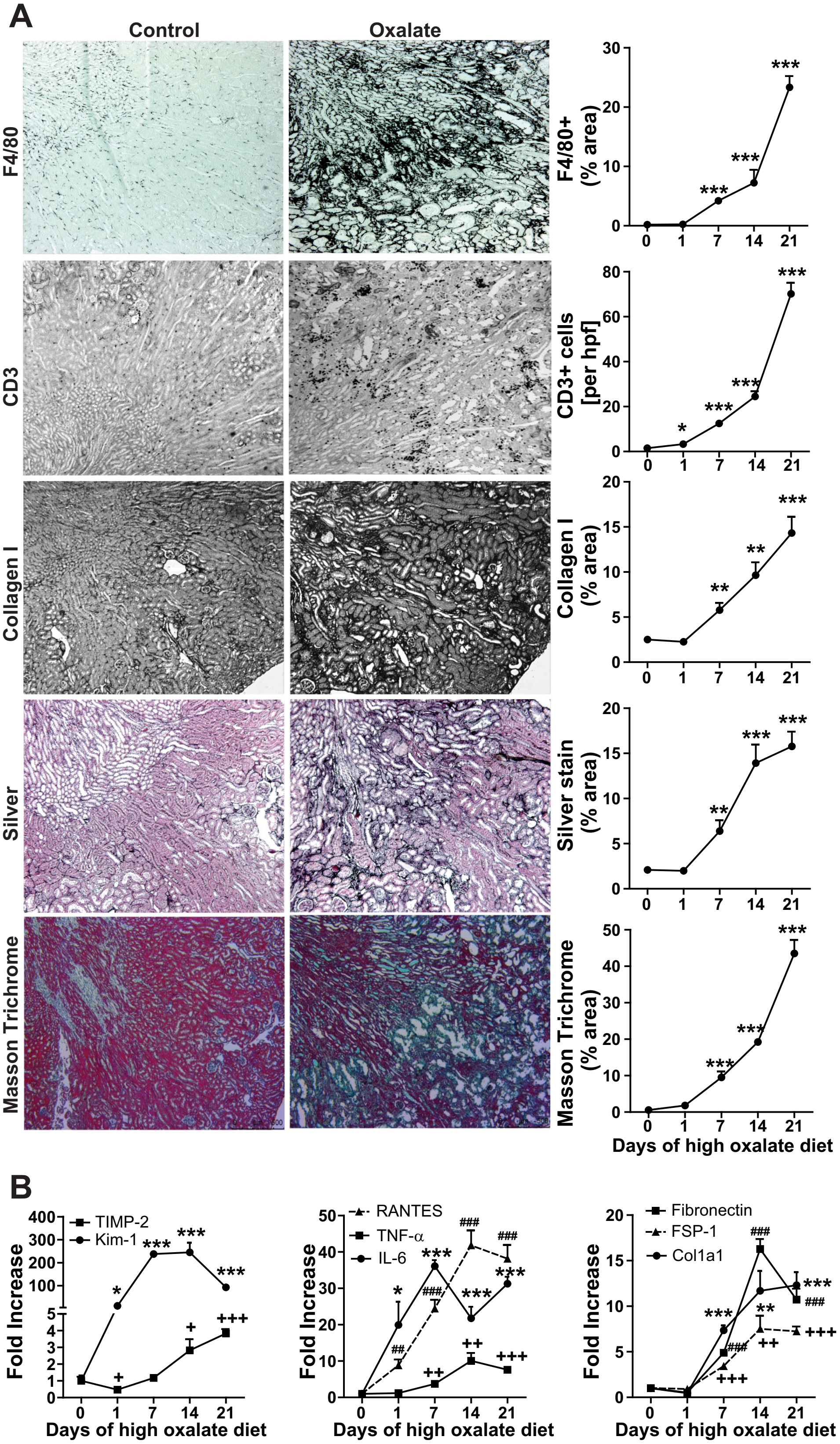

Fig. 3. Pathology of oxalate-induced CKD in male mice. C57BL/6 male mice were fed either a high-oxalate or control diet for 21 days. *A*: F4/80, CD3, collagen I, silver, Masson trichrome staining and their quantification. *B*: gene expression of kidney injury (TIMP-2, Kim-1), inflammation (RANTES, TNF-α, IL-6), and fibrosis (fibronectin, FSP-1, Col1a1) was analyzed using RT-PCR at different time points. Values are means ± SE from 7–8 mice/group. $^{*}P < 0.05$, $^{**}P < 0.01$, and $^{***}P < 0.001$ vs. control group. $^{+}P < 0.05$, $^{++}P < 0.01$, and $^{+++}P < 0.001$ vs. control group. $^{\#\#}P < 0.01$ and $^{\#\#\#}P < 0.001$ vs. control group.

area. For qualitative electron microscopic investigations of the hearts, several semithin and ultrathin sections were prepared and stained with methylene blue or uranyl acetate/lead citrate, respectively. Images of ultrathin sections were taken with a Zeiss electron microscope LEO EM 910 (Zeiss, Oberkochen, Germany).

Preparation of femoral bones. Femoral bones were removed, weighed, and fixed overnight using 1% (wt/vol) PFA buffered with PBS (pH 7.4). Bones were decalcified in 10% (wt/vol) EDTA solution (pH 7.4) before they were dehydrated and embedded in paraffin. Tissues were cut into 2-μm sections and stained with hematoxylin and eosin (H&E). Images were taken using a BX60 Olympus microscope equipped with a XC 30 camera (Olympus, Hamburg, Germany).

Statistical analysis. Student's *t*-test was used to generate *P* values.

RESULTS

A diet high in soluble oxalate induces stable CKD. Previous work from our groups suggests that intraperitoneal (ip) oxalate can induce acute kidney injury (22), and a high-oxalate diet can cause progressive renal failure (15). In the present study, we first examined the effects of the duration of feeding a soluble oxalate diet on renal function in C57BL/6 mice. Providing an oxalate diet induced a decline in GFR and an increase in plasma BUN and creatinine (Fig. 1, *A–C*). A shorter duration of oxalate feeding followed by a switch to a control diet induced less advanced stages of CKD as defined by GFR, plasma BUN, and creatinine (Fig. 1, *D–F*). Serial monitoring documented that these parameters peaked at the end of oxalate feeding, followed by mild recovery over the following 2-wk period. Urinary oxalate increased following a switch to a soluble oxalate compared with a control diet (Fig. 1*G*), but no renal or bladder stones were detected (images not shown). Similarly, we observed a sharp increase in plasma oxalate levels followed by a reduction in plasma oxalate levels when mice were switched back to a control diet (Fig. 1*H*). Therefore, while a diet high in soluble oxalate was found to induce a progressive decline in renal function as previously reported (13), these results show for the first time that it can also be used to induce stable CKD after dietary oxalate is discontinued.

Renal pathology of oxalate-induced CKD. As progressive scarring and fibrotic processes are a hallmark of CKD irrespective of the initiating disease, we next examined renal histology of mice fed a soluble oxalate diet for various durations. PAS staining revealed progressive tubular atrophy (Fig. 2*A*), result-

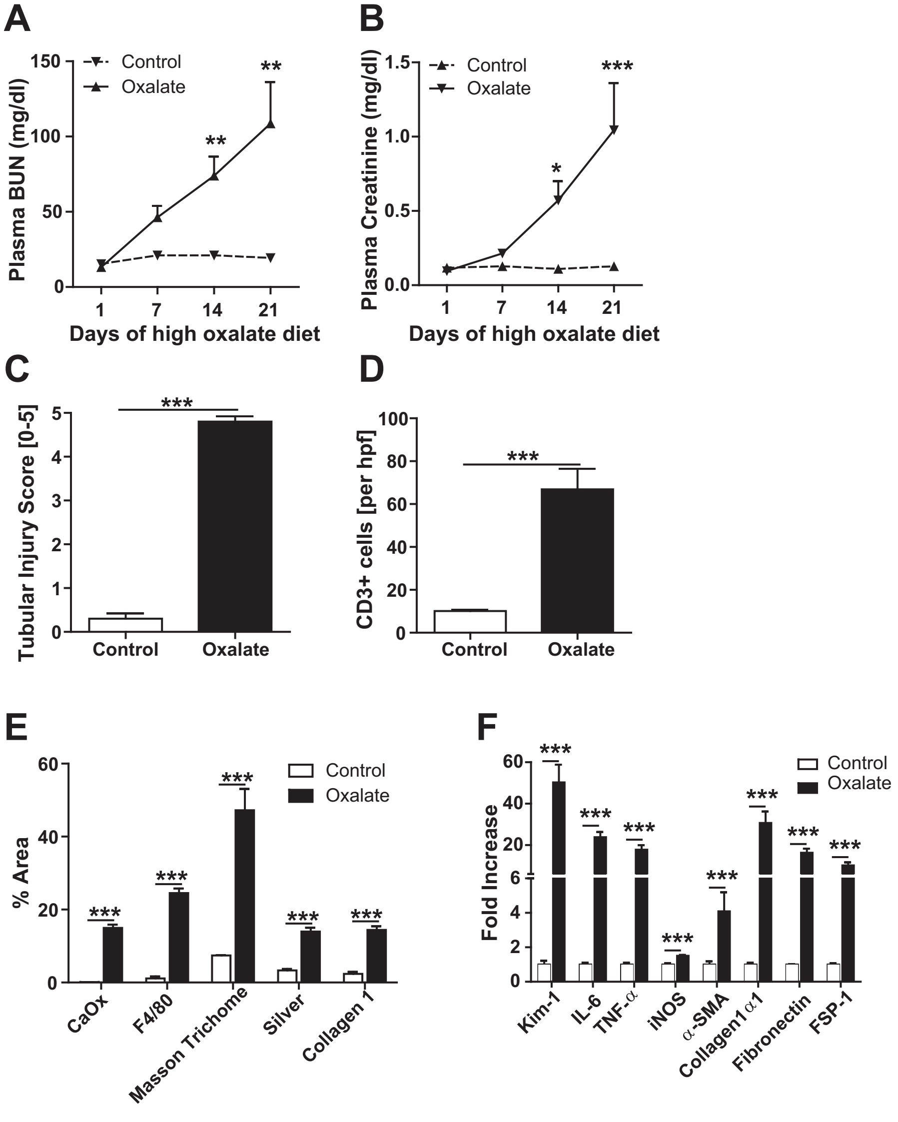

Fig. 4. Oxalate-induced CKD in female mice. C57BL/6 female mice were fed either a high-oxalate or control diet for 21 days. Note that female mice develop comparable CKD to male mice. *A*: plasma BUN levels. *B*: plasma creatinine levels. *C*: quantification of tubular injury. *D*: quantification of CD3+ve cells. *E*: quantification of CaOx crystal deposits, F4/80+ve macrophages, Masson trichrome, silver, and Collagen I+ve area. *F*: mRNA expression of kidney injury markers, proinflammatory genes, and profibrotic genes. Values are means ± SE from 7–8 mice/group. $^{*}P < 0.05$, $^{**}P < 0.0{,}1$ and $^{***}P < 0.001$ vs. control group.

ing in remnant atubular glomeruli (Fig. 2*B*) (2, 17). In addition, infiltration by macrophages/monocytes and T cells was observed, mainly in areas of interstitial fibrosis (Fig. 3*A*). Furthermore, progressive renal fibrosis was demonstrated as measured by collagen I, silver, and trichrome staining, and the duration of feeding allowed titration of the degree of parenchymal loss (Fig. 3*A*). Expression profiling for markers of kidney injury, inflammation and fibrosis, were consistent with progressive kidney atrophy (Fig. 3*B*). Female C57BL/6 mice revealed similar findings with very low interindividual vari-

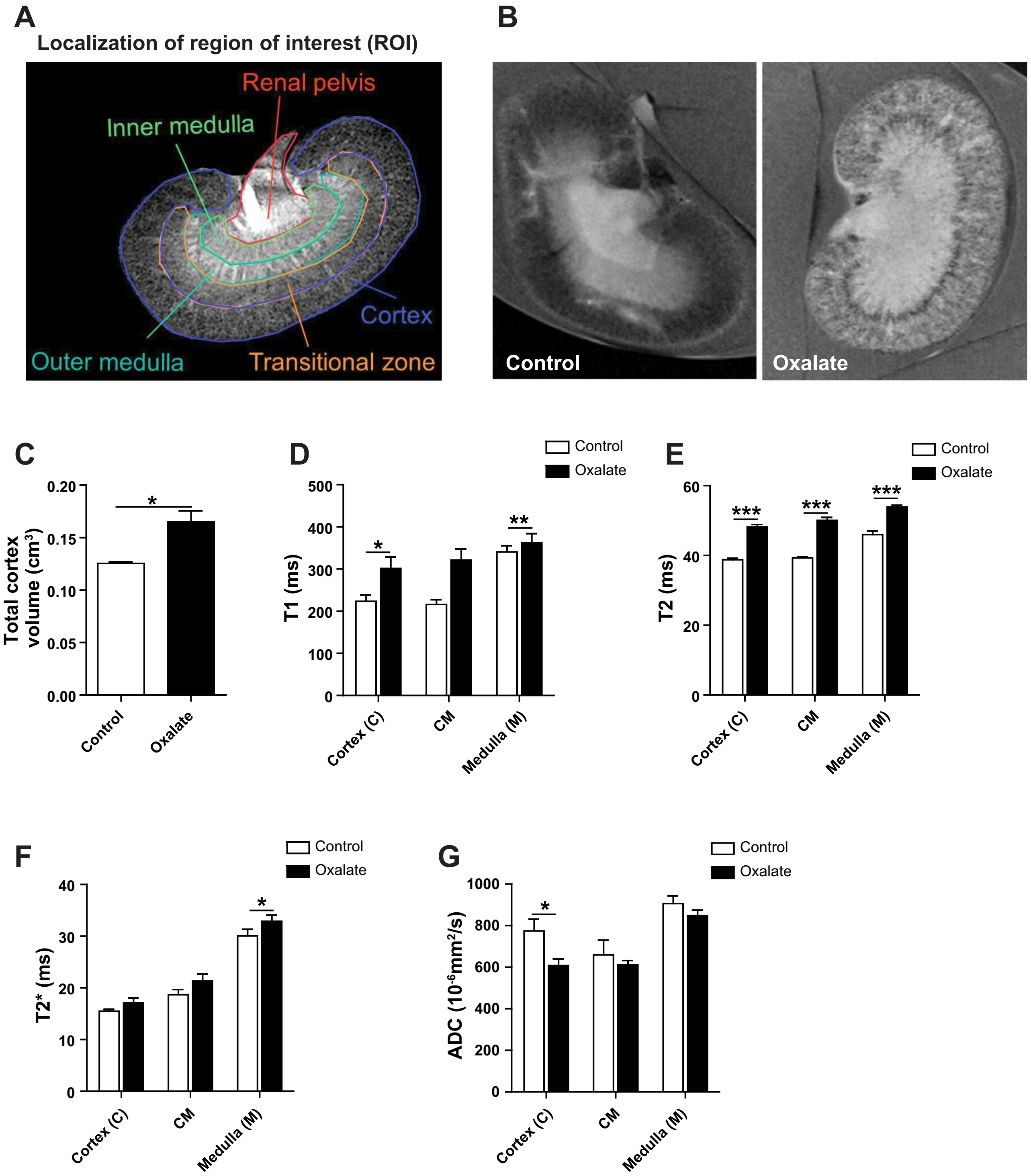

Fig. 5. MRI of oxalate-induced CKD. MRI was performed on kidneys of C57BL/6 male mice fed either a high-oxalate or control diet for 21 days. *A* and *B*: in representative morphological images, contrast characteristics of kidneys in the cortex, medulla, and transitional zone could be visualized. *C–G*: quantitative parameters of total cortex volume (*C*), T1 relaxation time (*D*), T2 relaxation time (*E*), T2* relaxation time (*F*), and apparent diffusion coefficient (ADC; *G*) showed significant differences between the groups in cortex (C), medulla (M), or transitional zone (CM). Values are means ± SE from 7–8 mice/group. $^{*}P < 0.05$, $^{**}P < 0.01$, and $^{***}P < 0.001$ vs. control group.

ability (Fig. 4, *A–F*). Given the increasing use of diagnostic imaging modalities to assess changes in renal morphology, we performed MRI of kidneys from mice. Compared with mice receiving a control diet, animals receiving an oxalate diet displayed an increase in kidney cortex volume, T1, T2, and T2* relaxation times, as well as a reduction in the apparent diffusion coefficient in the cortex (Fig. 5). These significant differences in the cortex are known to be associated with inflammation (increased volume and T2 time) and fibrosis (increased T1 time and decreased diffusion) and are consistent with findings from histology and expression profiling (25). Taken together, these data indicate that a high-oxalate diet induces CKD in male and female C57BL/6 mice characterized by progressive kidney atrophy and fibrosis.

Oxalate-induced CKD in C57BL/6 mice demonstrates classic CKD complications. We next examined whether the mouse model displays human CKD complications. An oxalate diet induced normochromic anemia (Fig. 6*A*) without affecting other blood cell lines (Supplementary Table 1; all supplementary data are accessible on the journal web site). CKD-related mineral bone disease (CKD-MBD) was demonstrated by elevated plasma FGF23 and PTH levels as well as hyperphosphatemia and hyperkalemia (Fig. 6, *B–E*) in addition to metabolic acidosis (Fig. 6*F*). Bone marrow of femoral bones demonstrated no oxalate crystal deposition of mice receiving an oxalate diet (Fig. 6*G*). Furthermore, an oxalate diet induced arterial hypertension (Fig. 7, *A* and *B*), which persisted after cessation of the oxalate-rich diet (Fig. 7, *C* and *D*). In addition, oxalate feeding induced cardiac fibrosis (Fig. 7, *E* and *F*), another serious cardiovascular complication of CKD. Electron microscopy demonstrated fibroblast activation in mice receiving an oxalate diet, as demonstrated by an increase in size and vacuolization of fibroblasts compared with mice receiving a control diet (Fig. 7*G*, white arrows). Similar to our observation in femoral bones, we could not detect any oxalate crystal deposition in heart tissue, arguing against systemic oxalosis to explain the observed phenotype.

Thus this model of oxalate diet-induced CKD presents with a wide spectrum of clinically established CKD complications.

It is of interest to compare the features of this oxalate-induced model of CKD with previous models of CKD, as summarized in Table 2.

DISCUSSION

The model of unilateral ureteral obstruction (UUO) has become a widely used model for studying CKD and fibrosis

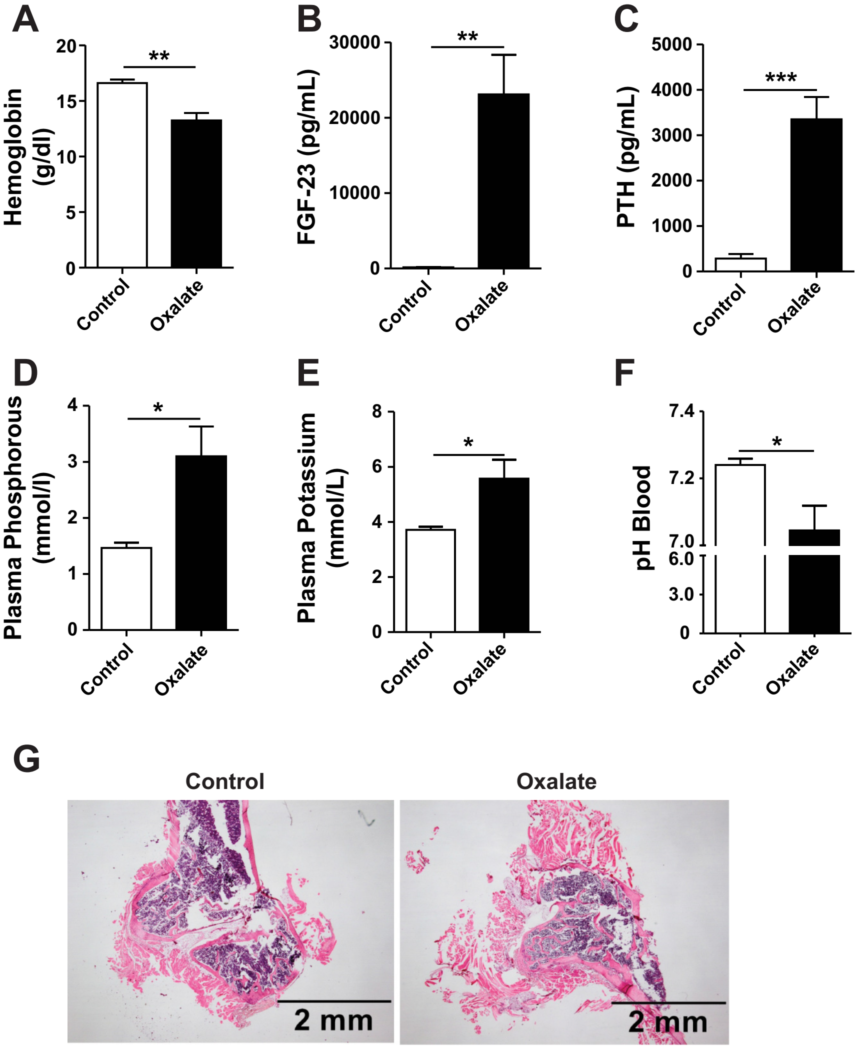
Fig. 6. Oxalate-induced CKD demonstrates classic CKD complications. *A–F*: C57BL/6 male mice were fed either a high-oxalate or control diet for 21 days, and different parameters for CKD complications were analyzed. *A*: hemoglobin levels in blood. *B*: plasma FGF-23 levels. *G*: plasma parathyroid hormone (PTH) levels. *D*: plasma phosphorous levels. *E*: plasma potassium levels. *F*: pH of blood. *G*: hematoxylin and eosin (HE) staining of femoral bones. Values are means ± SE from 4–5 mice/group. $^{*}P < 0.05$, $^{**}P < 0.01$, and $^{***}P < 0.001$ vs. control group.

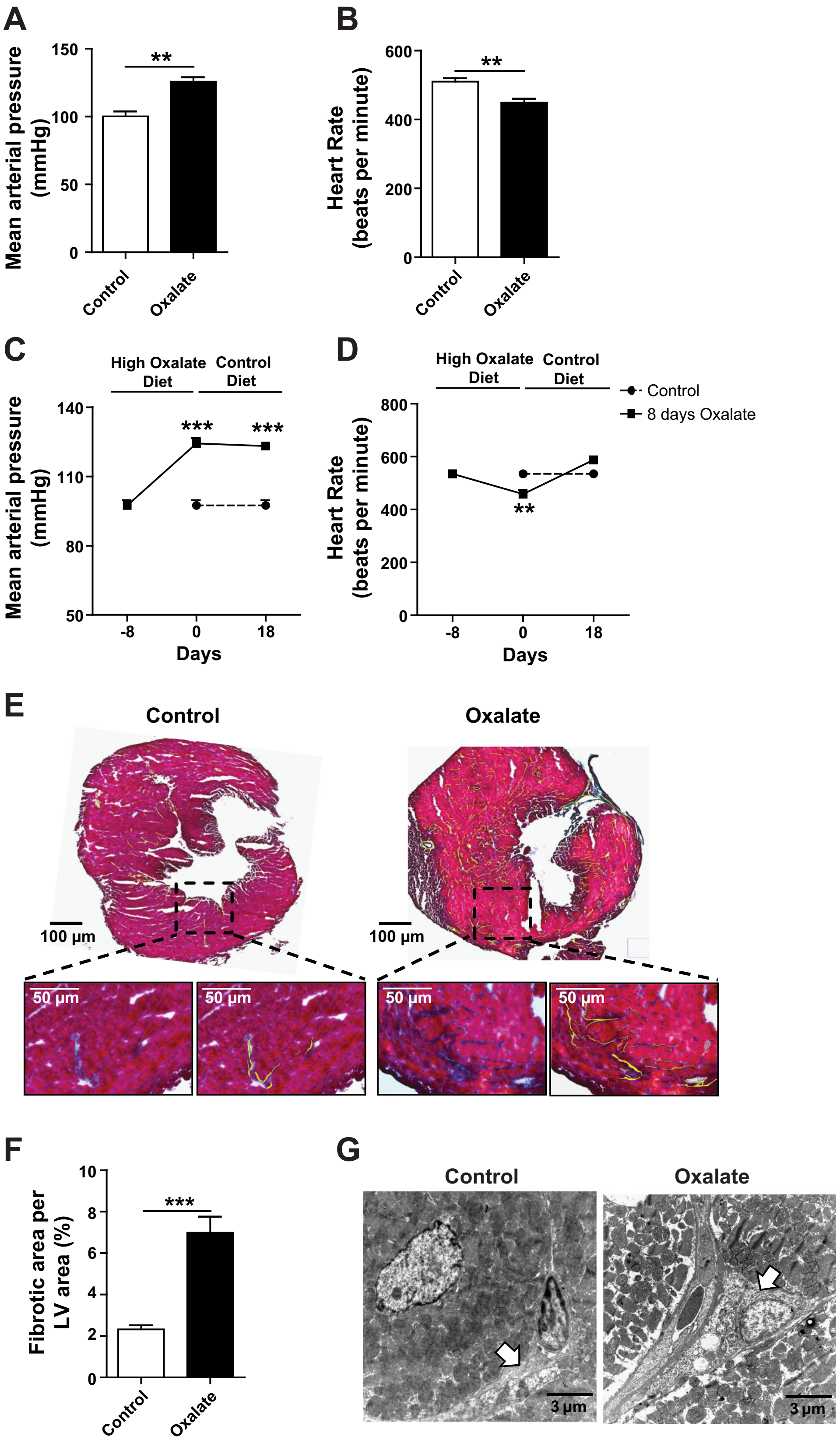

Fig. 7. Oxalate-induced CKD demonstrates hypertension and cardiac fibrosis. *A*: mean arterial blood pressure. *B*: heart rate. *C* and *D*: C57BL/6 male mice received a high-oxalate diet for 8 days and thereafter a control diet for 10 days. *C*: mean arterial blood pressure. *D*: heart rate. *E* and *F*: cardiac fibrosis was quantified (*F*) on Masson trichrome staining of heart cross sections (*E*) at *day 21* after a high-oxalate diet. *G*: electron microscopy of heart sections. Values are means ± SE from 4–5 mice/group except for $n = 2$ at *day 18* (control diet-fed group) in *C* and *D*. $*P < 0.05$, $**P < 0.01$, and $***P < 0.001$ vs. control group.

Table 2. *Comparison of murine CKD models*

CKD Animal Model	1	2	3	4	5	6	7	8	References
Unilateral ureteral obstruction (UUO)	✓	✓	✓		✓				3, 29
Surgical renal mass ablation (5/6 nephrectomy)	✓	✓			✓			✓	16, 18
Adenine-induced CKD	✓	✓		✓		✓	✓		7, 13, 19, 27, 28, 32
Aristolochic acid-induced CKD	✓	✓	✓	✓		✓	✓		6, 12
Folic acid-induced CKD	✓			✓	?	✓	✓	?	8, 30, 31
Oxalate-induced CKD	✓	✓	✓	✓	✓	✓	✓	✓	

CKD, chronic kidney disease. Criteria: 1, inducible in C57BL/6 mice; 2, reliable induction of stable CKD; 3, requires relatively short time to induce CKD and thus limits the burden for animals and reduces housing costs; 4, avoids surgical interventions, thus minimizing animal distress and use of painkillers; 5, inducible in male and female mice with low interindividual variability; 6, avoids reduction in renal mass; 7, reduction in glomerular filtration rate (GFR); 8, CKD complications such as normochromic anemia, hyperphosphatemia, hyperparathyroidism, hyperkalemia, acidosis, hypertension, and cardiovascular disease.

(3). While the model causes extensive parenchymal damage, functional compensation by the intact contralateral kidney prevents a significant change in renal function and the development of CKD complications (29). Absence of urine from the damaged kidney precludes biomarker discovery studies. In contrast, the oxalate diet-induced CKD model enables study of renal fibrosis while providing a functional end point of renal function as changes in GFR, serum BUN, and creatinine can be measured. It also allows the collection of urine and demonstrates established CKD complications.

The renal mass reduction models have been a mainstay of CKD studies (16). Unilateral nephrectomy is followed by either partial infarction or amputation of the poles of the remaining kidney, resulting in glomerular and tubule-interstitial injury. A strong limitation of the model is the need for two surgical interventions requiring microsurgery training, confounding effects related to anesthesia as well as surgical procedures, and the model's reproducibility and variability (16). In addition, performing a 5/6 nephrectomy limits the tissue available for analysis. After 16 wk, the C57BL/6 mice demonstrate increased albuminuria without increased blood pressure and without development of cardiac fibrosis unless angiotensin II is administered (18). The oxalate diet-induced model requires no microsurgery training/intervention, maintains sufficient renal tissue for analysis, and reliably induces CKD complications.

The adenine-induced model of CKD, unlike UUO or renal mass reduction, does not require surgery. It has largely been established in rats (32) as it is not easily adapted to mice given their reluctance to consume adenine. Addition of casein appears to blunt the smell and taste of adenine, to apply the approach to mice (13). Male mice present a more severe renal phenotype compared with female mice, presumably secondary to gender differences in the metabolism of adenine (7, 27). In addition, the model requires diets of different adenine content (13) or induction for 6 wk (28). Most strikingly, the mice develop profound hypotension compared with mice receiving a control diet (19) In contrast, oxalate is readily eaten by mice; the amount of dietary intake can be precisely monitored by measuring urinary oxalate excretion. Additional benefits include the short time frame of 1–3 wk for the induction of moderate to advanced CKD, which accelerates scientific workflow and reduces housing costs. Most strikingly, the oxalate model induces reliable and profound hypertension, an established complication of CKD in humans.

The aristolochic acid model represents an additional tool for investigating mechanisms of CKD progression and accessing potential interventions (6, 12). Aristolochic acid I (AAI) is the active ingredient implicated in Chinese herb nephropathy. Injection (ip) of AAI weekly has been shown to lead to progressive fibrosis and kidney failure that is more severe in male than female mice (6, 12), similar to observations made in the adenine model. No significant hypertension ensues (12). Contrary to the AAI model, the oxalate diet-induced model avoids direct handling and injections of mice. As the oxalate model works in male and female mice, it allows examination of gender differences in response to pharmaceutical interventions to treat CKD, providing a platform to use both male and female mice in preclinical studies as requested by the National Institutes of Health (4). In addition, gender-restricted models produce excess pups, which are avoided when both males and females can be used for experimentation, and the low interindividual variability allows smaller group sizes.

The folic acid nephropathy model induces interstitial fibrosis following ip injection of a high dosage of folic acid. The advantage of this model compared with the UUO model is that renal function can be assessed. However, the model requires ip injections compared with the oxalate feeding model, is somewhat variable, and yet to be characterized in regards to gender differences and CKD complications (8, 30, 31).

Despite the advantages of the oxalate model over previous CKD models, a number of limitations have to be considered. Oxalate crystals primarily induce tubular injury (20–22), while many forms of human CKD are primarily driven by podocyte loss (5). The mechanism of crystal-induced progression may not translate to all forms of CKD. However, the extensively studied adenine and folic acid models are similarly crystal induced (19). Similarly, one may argue that UUO, as the benchmark model of fibrosis associated with an increase in vascular resistance and a reduced blood flow following surgery, provides a mechanism of fibrosis not mimicking the pathophysiology of common forms of CKD (14).

Nevertheless, several elements of the oxalate model, including tubular atrophy, renal inflammation, and fibrosis, are common to many forms of CKD. In addition, one of the major strengths of the model is the reproducibility of CKD complications, thereby allowing study of the mechanisms of FGF23 activation, hyperphosphatemia, hyperparathyroidism, hypertension, and cardiac fibrosis. Moreover, increasing the number of CKD models available may help to validate important findings and improve standards.

In conclusion, feeding a soluble oxalate diet represents a simple, reproducible, and technically undemanding CKD model providing functional data in male as well as female C57BL/6 mice. Moreover, the duration of feeding enables titrated induction of various stages of CKD associated with numerous clinically important CKD complications. Thus the oxalate diet-induced CKD model offers novel opportunities for CKD research.

ACKNOWLEDGMENTS

We thank Jana Mandelbaum, Dan Draganovic, Nada Cordasic, Sebastian Kaidel, Monika Klewer, and Silvia Crowley for expert technical assistance.

Parts of this work were presented in the thesis project of J. N. Eberhard. at the Medical Faculty of the University of Munich.

GRANTS

This work was supported by grants from the Deutsche Forschungsgemeinschaft to H. J. Anders (AN372/16-1) and F. Knauf (KN 1148/2-1), by the German Federal Ministry of Education and Research (Infrafrontier grant 01KX1012) to M. H. de Angelis, and the Interdisciplinary Center for Clinical Research (University Hospital Erlangen) and TRENAL program by the German Academic Exchange Service to V. Pfann.

DISCLOSURES

No conflicts of interest, financial or otherwise, are declared by the authors.

AUTHOR CONTRIBUTIONS

Author contributions: S.R.M., J.N.E., V.P., J.A.M., M.N.D., C.D., S.R., J.D., E.W., M.H.d.A., C.A.W., K.A., K.-U.E., P.S.A., H.J.A., and F.K. provided conception and design of research; S.R.M., J.N.E., V.P., J.A.M., M.N.D., C.D., S.R., J.D., M.G., S.V.K., B.R., E.W., M.H.d.A., T.B., B.D., C.A.W., H.J.A., and F.K. performed experiments; S.R.M., J.N.E., V.P., J.A.M., M.N.D., C.D., S.R., J.D., M.G., S.V.K., B.R., E.W., M.H.d.A., T.B., B.D., C.A.W., K.A., P.S.A., H.J.A., and F.K. analyzed data; S.R.M., J.N.E., V.P., J.A.M., M.N.D., C.D., S.R., J.D., M.G., S.V.K., B.R., E.W., M.H.d.A., T.B., B.D., C.A.W., K.A., P.S.A., H.J.A., and F.K. interpreted results of experiments; S.R.M., J.N.E., V.P., M.N.D., C.D., S.R., J.D., M.H.d.A., T.B., B.D., H.J.A., and F.K. prepared figures; S.R.M., J.N.E., V.P., M.N.D., M.H.d.A., C.A.W., K.A., P.S.A., H.J.A., and F.K. drafted manuscript; S.R.M., J.N.E., V.P., C.A.W., K.A., K.-U.E., P.S.A., H.J.A., and F.K. edited and revised manuscript; S.R.M., J.N.E., V.P., M.N.D., S.R., J.D., S.V.K., C.A.W., K.A., K.-U.E., P.S.A., H.J.A., and F.K. approved final version of manuscript.

REFERENCES

1. **Becker GJ, Hewitson TD.** Animal models of chronic kidney disease: useful but not perfect. *Nephrol Dial Transplant* 28: 2432–2438, 2013.
2. **Chevalier RL, Forbes MS.** Generation and evolution of atubular glomeruli in the progression of renal disorders. *J Am Soc Nephrol* 19: 197–206, 2008.
3. **Chevalier RL, Forbes MS, Thornhill BA.** Ureteral obstruction as a model of renal interstitial fibrosis and obstructive nephropathy. *Kidney Int* 75: 1145–1152, 2009.
4. **Clayton JA, Collins FS.** Policy: NIH to balance sex in cell and animal studies. *Nature* 509: 282–283, 2014.
5. **Collins AJ, Foley RN, Chavers B, Gilbertson D, Herzog C, Ishani A, Johansen K, Kasiske BL, Kutner N, Liu J, St Peter W, Guo H, Hu Y, Kats A, Li S, Li S, Maloney J, Roberts T, Skeans M, Snyder J, Solid C, Thompson B, Weinhandl E, Xiong H, Yusuf A, Zaun D, Arko C, Chen SC, Daniels F, Ebben J, Frazier E, Johnson R, Sheets D, Wang X, Forrest B, Berrini D, Constantini E, Everson S, Eggers P, Agodoa L.** US Renal Data System 2013. Annual Data Report. *Am J Kidney Dis* 63: A7, 2014.
6. **Dai XY, Zhou L, Huang XR, Fu P, Lan HY.** Smad7 protects against chronic aristolochic acid nephropathy in mice. *Oncotarget* 6: 11930–11944, 2015.
7. **Diwan V, Small D, Kauter K, Gobe GC, Brown L.** Gender differences in adenine-induced chronic kidney disease and cardiovascular complications in rats. *Am J Physiol Renal Physiol* 307: F1169–F1178, 2014.
8. **Fink M, Henry M, Tange JD.** Experimental folic acid nephropathy. *Pathology* 19: 143–149, 1987.
9. **Fiske CH, Subbarow Y.** The colorimetric determination of phosphorous. *J Biol Chem* 66: 375–400, 1925.
10. **Fiske CH, Subbarow Y.** The nature of the "inorganic phosphate" in voluntary muscle. *Science* 65: 401–403, 1927.
11. **Hennedige T, Koh TS, Hartono S, Yan YY, Song IC, Zheng L, Lee WS, Rumpel H, Martarello L, Khoo JB, Koh DM, Chuang KH, Thng CH.** Intravoxel incoherent imaging of renal fibrosis induced in a murine model of unilateral ureteral obstruction. *Magn Reson Imaging* 33: 1324–1328, 2015.
12. **Huang L, Scarpellini A, Funck M, Verderio EA, Johnson TS.** Development of a chronic kidney disease model in C57BL/6 mice with relevance to human pathology. *Nephron Extra* 3: 12–29, 2013.
13. **Jia T, Olauson H, Lindberg K, Amin R, Edvardsson K, Lindholm B, Andersson G, Wernerson A, Sabbagh Y, Schiavi S, Larsson TE.** A novel model of adenine-induced tubulointerstitial nephropathy in mice. *BMC Nephrol* 14: 116, 2013.
14. **Kim W, Moon SO, Lee SY, Jang KY, Cho CH, Koh GY, Choi KS, Yoon KH, Sung MJ, Kim DH, Lee S, Kang KP, Park SK.** COMP-angiopoietin-1 ameliorates renal fibrosis in a unilateral ureteral obstruction model. *J Am Soc Nephrol* 17: 2474–2483, 2006.
15. **Knauf F, Asplin JR, Granja I, Schmidt IM, Moeckel GW, David RJ, Flavell RA, Aronson PS.** NALP3-mediated inflammation is a principal cause of progressive renal failure in oxalate nephropathy. *Kidney Int* 84: 895–901, 2013.
16. **Kren S, Hostetter TH.** The course of the remnant kidney model in mice. *Kidney Int* 56: 333–337, 1999.
17. **Lech M, Grobmayr R, Ryu M, Lorenz G, Hartter I, Mulay SR, Susanti HE, Kobayashi KS, Flavell RA, Anders HJ.** Macrophage phenotype controls long-term AKI outcomes–kidney regeneration versus atrophy. *J Am Soc Nephrol* 25: 292–304, 2014.
18. **Leelahavanichkul A, Yan Q, Hu X, Eisner C, Huang Y, Chen R, Mizel D, Zhou H, Wright EC, Kopp JB, Schnermann J, Yuen PS, Star RA.** Angiotensin II overcomes strain-dependent resistance of rapid CKD progression in a new remnant kidney mouse model. *Kidney Int* 78: 1136–1153, 2010.
19. **Mishima E, Fukuda S, Shima H, Hirayama A, Akiyama Y, Takeuchi Y, Fukuda NN, Suzuki T, Suzuki C, Yuri A, Kikuchi K, Tomioka Y, Ito S, Soga T, Abe T.** Alteration of the intestinal environment by lubiprostone is associated with amelioration of adenine-induced CKD. *J Am Soc Nephrol* 26: 1787–1794, 2015.
20. **Mulay SR, Desai J, Kumar SV, Eberhard JN, Thomasova D, Romoli S, Grigorescu M, Kulkarni OP, Popper B, Vielhauer V, Zuchtriegel G, Reichel C, Bräsen JH, Romagnani P, Bilyy R, Munoz LE, Herrmann M, Liapis H, Krautwald S, Linkermann A, Anders HJ.** Cytotoxicity of crystals involves RIPK3-MLKL-mediated necroptosis. *Nat Commun* 28: 10274, 2016.
21. **Mulay SR, Evan A, Anders HJ.** Molecular mechanisms of crystal-related kidney inflammation and injury. Implications for cholesterol embolism, crystalline nephropathies and kidney stone disease. *Nephrol Dial Transplant* 29: 507–514, 2014.
22. **Mulay SR, Kulkarni OP, Rupanagudi KV, Migliorini A, Darisipudi MN, Vilaysane A, Muruve D, Shi Y, Munro F, Liapis H, Anders HJ.** Calcium oxalate crystals induce renal inflammation by NLRP3-mediated IL-1beta secretion. *J Clin Invest* 123: 236–246, 2013.
23. **Rathkolb B, Fuchs H, Gailus-Durner V, Aigner B, Wolf E, Hrabe de Angelis M.** Blood collection from mice and hematological analyses on mouse blood. *Curr Protoc Mouse Biol* 3: 101–119, 2013.
24. **Rathkolb B, Hans W, Prehn C, Fuchs H, Gailus-Durner V, Aigner B, Adamski J, Wolf E, Hrabe de Angelis M.** Clinical chemistry and other laboratory tests on mouse plasma or serum. *Curr Protoc Mouse Biol* 3: 69–100, 2013.
25. **Salerno M, Kramer CM.** Advances in parametric mapping with CMR imaging. *JACC Cardiovasc Imaging* 6: 806–822, 2013.
26. **Schreiber A, Shulhevich Y, Geraci S, Hesser J, Stsepankou D, Neudecker S, Koenig S, Heinrich R, Hoecklin F, Pill J, Friedemann J, Schweda F, Gretz N, Schock-Kusch D.** Transcutaneous measurement of renal function in conscious mice. *Am J Physiol Renal Physiol* 303: F783–F788, 2012.
27. **Stockelman MG, Lorenz JN, Smith FN, Boivin GP, Sahota A, Tischfield JA, Stambrook PJ.** Chronic renal failure in a mouse model of human adenine phosphoribosyltransferase deficiency. *Am J Physiol Renal Physiol* 275: F154–F163, 1998.
28. **Tanaka T, Doi K, Maeda-Mamiya R, Negishi K, Portilla D, Sugaya T, Fujita T, Noiri E.** Urinary L-type fatty acid-binding protein can reflect renal tubulointerstitial injury. *Am J Pathol* 174: 1203–1211, 2009.
29. **Ucero AC, Benito-Martin A, Izquierdo MC, Sanchez-Nino MD, Sanz AB, Ramos AM, Berzal S, Ruiz-Ortega M, Egido J, Ortiz A.** Unilateral ureteral obstruction: beyond obstruction. *Int Urol Nephrol* 46: 765–776, 2014.
30. **Yang HC, Fogo AB.** Mechanisms of disease reversal in focal and segmental glomerulosclerosis. *Adv Chronic Kidney Dis* 21: 442–447, 2014.
31. **Yang HC, Zuo Y, Fogo AB.** Models of chronic kidney disease. *Drug Disc Today Dis Models* 7: 13–19, 2010.
32. **Yokozawa T, Zheng PD, Oura H, Koizumi F.** Animal model of adenine-induced chronic renal failure in rats. *Nephron* 44: 230–234, 1986.